 CMC, vol.34, no.3, pp.177-198, 2013

Corotational Formulation of Reduced Order Homogenization

V. Filonova[1], Y. Liu[1], M. Bailakanavar[1], J. Fish[1], Z. Yuan[2]

Abstract: A corotational formulation for reduced order homogenization is presented. While in principle the proposed method is valid for problems with arbitrary large strains, it is computational advantageous over the classical direct computational homogenization method for large rotations but moderate unit cell distortions. We validate the method for several large deformation problems including: (i) hat-section composite beam with two-dimensional chopped tow composite architecture, (ii) polyethylene microstructure consisting of 'hard' and 'soft' domains (segments), and (iii) fiber framework called fiberform either embedded or not in an amorphous matrix.

Keywords: Corotational frame, reduced order homogenization, large deformations

1 Introduction

In this manuscript we focus on extending the reduced order homogenization [Oskay and Fish (2008); Oskay and Fish (2007); Yuan and Fish (2009)a; Yuan and Fish (2009)b; Fish and Yuan (2009), Fish, Filonova and Yuan (2013)] to large deformation problems. The general framework of reduced order homogenization for large deformation problems in periodic inelastic heterogeneous medium has been given in [Fish and Shek (2000)]. In the following we describe a simplified variant based on the corotational formulation. The corotational framework allows to: (i) take advantage of the precomputed influence functions prior nonlinear analysis and (ii) incorporate nonlinear geometrical information using conventional corotational finite element code architecture.

Development of the corotational formulation has been actively pursued in early 1980s. Important papers are those of Argyris (1982), Belytschko and Hsieh (1973),

[1] Columbia University, New York, NY, U.S.A.
[2] Multiscale Design Systems, Loudonville, NY, U.S.A.

Bergan and Horrigmoe (1976). In the following, we focus on the specificities of the corotational approach applied to the two-scale reduced order homogenization.

In the corotational formulation the motion of a heterogeneous body is decomposed into rigid body motion (rotation and translation) followed by deformational displacements. In the spatially discretized domain, this decomposition can be accomplished by attaching a local corotational coordinate frame to either each finite element or each *unit cell* and assuming that deformational displacements are small. Here, the latter is pursued.

The manuscript is organized as follows. The formulation of the reduced order homogenization method is outlined in Section 2. Section 3 presents several validation examples for large deformation problems including: (i) two-dimensional chopped tow composites employed in automotive applications, (ii) polyethylene microstructure consisting of 'hard' and 'soft' domains (segments) employed for energy absorption in military and industrial applications, and (iii) fiber framework called fiberform either embedded or free from an amorphous matrix used as heat shield on space crafts to prevent structural damage during reentry into the atmosphere.

2 Formulation of the reduced order homogenization for large deformation problems

Consider large deformation governing equations for the composite domain in the current (deformed) configuration

$$\begin{aligned}
&\sigma^{\zeta}_{ij,j}(\boldsymbol{x},t)+b^{\zeta}_{i}(\boldsymbol{x},t)=0\\
&\sigma^{\Re\zeta}_{ij}(\boldsymbol{x},t)=\Re^{\zeta}_{ki}(\boldsymbol{x},t)\ \Re^{\zeta}_{lj}(\boldsymbol{x},t)\ \sigma^{\zeta}_{kl}(\boldsymbol{x},t)\\
&\dot{\sigma}^{\Re\zeta}_{ij}=L^{\Re\zeta}_{ijkl}(x^{\Re}/\zeta)\left(\dot{\varepsilon}^{\Re\zeta}_{kl}(\boldsymbol{x},t)-\dot{\mu}^{\Re\zeta}_{kl}(\boldsymbol{x},t)\right)\\
&\dot{\varepsilon}^{\Re\zeta}_{kl}(\boldsymbol{x},t)=\tfrac{1}{2}\left(\frac{\partial v^{\Re\zeta}_{k}}{\partial x^{\Re}_{l}}+\frac{\partial v^{\Re\zeta}_{l}}{\partial x^{\Re}_{k}}\right)
\end{aligned} \tag{1}$$

where the total strain ε^{ζ}_{kl} is additively decomposed into elastic strain and inelastic strain or more generally referred to as eigenstrains μ^{ζ}_{kl}. The right superscript ζ indicates dependence on the fine-scale heterogeneity. The right superscript $\Re$ denotes various fields defined in the corotational coordinates $\boldsymbol{x}^{\Re}$ which is attached to the material microstructure and is related to the global coordinate system $\boldsymbol{x}$ by

$$x_i=\Re^{\zeta}_{ij}x^{\Re}_{j}+\hat{x}_i \tag{2}$$

$\Re^{\zeta}_{ij}$ denotes rigid body rotation of the corotational frame; and $\hat{x}_i$ is a centroid of the corotational frame, subsequently to be used as the unit cell centroid; the constitutive tensor $L^{\Re\zeta}_{ijkl}(\boldsymbol{x}^{\Re}/\zeta)$ is assumed to be periodic in the corotational frame; σ^{ζ}_{ij} is

Cauchy stress; $v_i^{\Re\zeta} = \dot{x}_i^{\Re\zeta}$ denotes velocity in the corotational frame; the time t here is used to track the load level. Superimposed dot denotes material time derivative.

The velocity field in the global Cartesian coordinates is expanded in the asymptotic expansion as

$$v_k^{\zeta}(\boldsymbol{x},t) \equiv v_k(\boldsymbol{x},\boldsymbol{y},t) = v_k^{(0)}(\boldsymbol{x},t) + \zeta v_k^{(1)}(\boldsymbol{x},\boldsymbol{y},t) + O(\zeta^2) \tag{3}$$

where $\boldsymbol{x}$ and $\boldsymbol{y}$ are coordinates corresponding to macro- and microscopic domains, respectively, as shown in Fig.1.

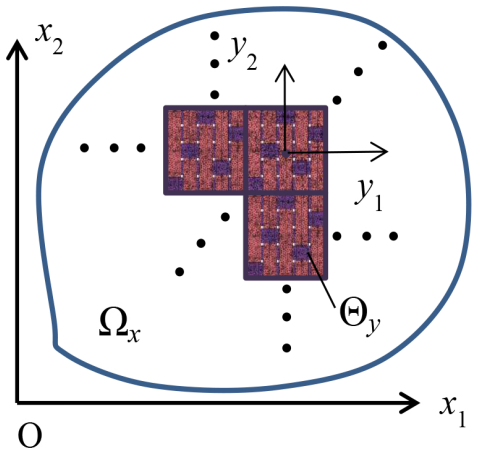

Figure 1: Periodic microstructure of the composite domain: Θ_y – unit cell domain; Ω_x – macroscopic domain.

Various terms in the asymptotic expansion of the velocity are expanded around the unit cell centroid $\hat{\boldsymbol{x}}$ in the current configuration where $\boldsymbol{x} - \hat{\boldsymbol{x}} = \zeta \boldsymbol{y}$, (see Fig. 2)

$$v_k^{\zeta}(\boldsymbol{x},t) \equiv v_k(\boldsymbol{x},\boldsymbol{y},t) = v_k^{(0)}(\hat{\boldsymbol{x}},t) + \zeta \left(v_k^{(1)}(\hat{\boldsymbol{x}},\boldsymbol{y},t) + v_{k,x_l}^{(0)}(\hat{\boldsymbol{x}},t)\Big|_{\hat{\boldsymbol{x}}} y_l \right) + O(\zeta^2) \tag{4}$$

We now define the unit cell corotational coordinate system $y_j^{\Re}$ placed at the unit cell centroid as

$$y_l = \Re_{lj}^{\zeta} y_j^{\Re} \tag{5}$$

It is convenient to express the velocity field in the corotational coordinate system as

$$v_i^{\Re\zeta}(\boldsymbol{x},t) \equiv v_i^{\Re}(\boldsymbol{x},\boldsymbol{y},t) = \Re_{ki}^{\zeta} v_k^{(0)}(\hat{\boldsymbol{x}},t) + \zeta \left(\Re_{ki}^{\zeta} v_k^{(1)}(\hat{\boldsymbol{x}},\boldsymbol{y},t) + \Re_{ki}^{\zeta} v_{k,x_l}^{(0)}(\hat{\boldsymbol{x}},t)\Big|_{\hat{\boldsymbol{x}}} y_l \right) + O(\zeta^2) \tag{6}$$

We now proceed by approximating $\Re_{ki}^{\zeta}$ as

$$\Re_{ki}^{\zeta}(\boldsymbol{x},t) \equiv \Re_{ki}(\boldsymbol{x},\boldsymbol{y},t) = \Re_{ki}^{c}(\hat{\boldsymbol{x}},t) + O(\zeta^2) \tag{7}$$

where $\Re_{ki}^{c}(\boldsymbol{x},t)$ denotes the coarse-scale rotation. By neglecting $O(\zeta^2)$ in Eq.(7) implies that all points in the unit cell have the same rotation (see Remark 1 and Fig. 2).

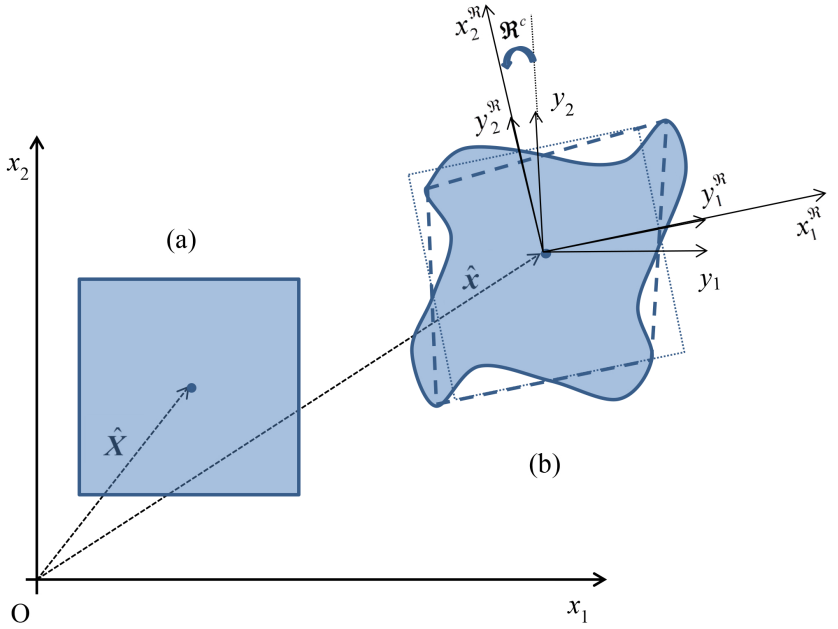

Figure 2: Unit cell distortion and rotation: (a) – initial configuration; (b) – current configuration.

Inserting Eq.(7) and Eq.(5) into Eq.(6) yields

$$\begin{aligned} v_i^{\Re\zeta}(\boldsymbol{x},t) = {} & \Re_{ki}^{c}(\hat{\boldsymbol{x}},t) v_k^{(0)}(\hat{\boldsymbol{x}},t) \\ & + \zeta \left(v_i^{\Re(1)}(\hat{\boldsymbol{x}},\boldsymbol{y},t) + \Re_{ki}^{c}(\hat{\boldsymbol{x}},t) \Re_{lj}^{c}(\hat{\boldsymbol{x}},t) v_{k,x_l}^{(0)}(\hat{\boldsymbol{x}},t) \Big|_{\hat{\boldsymbol{x}}} y_j^{\Re} \right) \\ & + O(\zeta^2) \end{aligned} \tag{8}$$

where $v_i^{\Re(1)}(\hat{\boldsymbol{x}},y,t) = \Re_{ki}^{c}(\hat{\boldsymbol{x}},t) v_k^{(1)}(\hat{\boldsymbol{x}},\boldsymbol{y},t)$ is the fine-scale correction in the corotational frame. Velocity gradient in the corotational frame follows from Eq.(8)

$$\frac{\partial v_i^{\Re\zeta}}{\partial x_j^{\Re}} = \frac{\partial v_i^{\Re(1)}(\hat{\boldsymbol{x}},\boldsymbol{y},t)}{\partial y_j^{\Re}} + \Re_{ki}^{c}(\hat{\boldsymbol{x}},t) \Re_{lj}^{c}(\hat{\boldsymbol{x}},t) v_{k,x_l}^{(0)}(\hat{\boldsymbol{x}},t) \Big|_{\hat{\boldsymbol{x}}} + O(\zeta) \tag{9}$$

The rate of deformation is obtained by taking symmetric part of velocity gradient

$$\dot{\varepsilon}_{ij}^{\Re\zeta}\left(\boldsymbol{x}^{\Re},t\right) = v^{\Re(1)}_{\left(i,y_j^{\Re}\right)}(\hat{\boldsymbol{x}},\boldsymbol{y},t) + \Re^{c}_{ki}(\hat{\boldsymbol{x}},t)\Re^{c}_{lj}(\hat{\boldsymbol{x}},t)v^{(0)}_{(k,x_l)}(\hat{\boldsymbol{x}},t)\,|_{\hat{\boldsymbol{x}}} + O(\zeta) \tag{10}$$

Let ${}_{n}u_i^{\Re}$ be converged displacement in the corotational frame at load increment n. We wish to find the displacement increment $\Delta u_i^{\Re}$ in the corotational frame by integrating Eq.(10) using midpoint integration rule to obtain second order accuracy

$$\int_{t_n}^{t_{n+1}} \dot{\varepsilon}_{ij}^{\Re\zeta}\left(\boldsymbol{x}^{\Re},t\right)\,dt \equiv \Delta\varepsilon_{ij}^{\Re\zeta} = \Delta\varepsilon_{ij}^{\Re f} + \zeta\Delta\varepsilon_{ij}^{\Re(1)} + O(\zeta^2) \tag{11}$$

where

$$\Delta\varepsilon_{ij}^{\Re f} = \Delta u^{\Re(1)}_{\left(i,y_j^{\Re}\right)}({}_{n+1/2}\hat{\boldsymbol{x}},\boldsymbol{y}) + \Re^{c}_{ki}({}_{n+1/2}\hat{\boldsymbol{x}})\Re^{c}_{lj}({}_{n+1/2}\hat{\boldsymbol{x}})\;sym\left(\frac{\partial\Delta u_k^{(0)}}{\partial_{n+1/2}x_l}\right)\Bigg|_{{}_{n+1/2}\hat{\boldsymbol{x}}} \tag{12}$$

The first term in Eq.(12) denotes the fine-scale perturbation of the displacement increment which is assumed to be small; the second term in Eq.(12) denotes the coarse-scale strain increment rotated into the corotational frame. Note that the coarse-scale strain increment can be large although fine-scale perturbations $\Delta u^{\Re(1)}_{\left(i,y_j^{\Re}\right)}$ are small. The unit cell coordinate of the centroid at the mid-step ${}_{n+1/2}\hat{\boldsymbol{x}}$ is defined as

$${}_{n+1/2}\hat{\boldsymbol{x}} = \frac{1}{2}\left({}_{n}\hat{\boldsymbol{x}} + {}^{i+1}_{n+1}\hat{\boldsymbol{x}}\right) \tag{13}$$

where the left superscript denotes Newton iteration count at the coarse-scale. The coarse-scale displacement increment $\Delta u_k^{(0)}$ and the fine-scale perturbation increment in the corotational frame $\Delta u_i^{\Re(1)}$ are defined as

$$\begin{aligned}\Delta u_k^{(0)} &= {}^{i+1}_{n+1}u_k^{(0)} - {}_{n}u_k^{(0)}\\ \Delta u_i^{\Re(1)} &= {}^{i+1}_{n+1}u_i^{\Re(1)} - {}_{n}u_i^{\Re(1)}\end{aligned} \tag{14}$$

Integrating Eq.(12) over the unit cell domain and exploiting solution periodicity in the corotational frame yields the coarse-scale strain increment

$$\Delta\varepsilon_{ij}^{\Re c} = \Re^{c}_{ki}({}_{n+1/2}\hat{\boldsymbol{x}})\Re^{c}_{lj}({}_{n+1/2}\hat{\boldsymbol{x}})\;sym\left(\frac{\partial\Delta u_k^{(0)}}{\partial_{n+1/2}x_l}\right)\Bigg|_{{}_{n+1/2}\hat{\boldsymbol{x}}} \tag{15}$$

It can be seen that the second term in Eq.(12) represents the average fine-scale strain increment.

We assume that the Cauchy stress is a function of the previously converged stress, ${}_n\sigma_{ij}^{\zeta}$, rotation $\Re_{lj}^{\zeta}$ and strain increment in the corotational frame $\Delta\varepsilon_{ij}^{\Re f}$, i.e. $\sigma_{ij}^{\zeta}\left({}_n\sigma_{ij}^{\zeta},\Re_{kl}^{\zeta},\Delta\varepsilon_{ij}^{\Re\zeta}\right)$. To derive the equilibrium equation we start by expanding Cauchy stress around $\left({}_n\sigma_{ij}^{\zeta},\Re_{kl}^{c},\Delta\varepsilon_{ij}^{\Re f}\right)$, which yields

$$\begin{aligned}\sigma_{ij}^{\zeta}\left({}_n\boldsymbol{\sigma}_{\zeta},\boldsymbol{\Re}_{\zeta},\Delta\boldsymbol{\varepsilon}_{\Re\zeta}\right) &= \sigma_{ij}^{\zeta}\left({}_n\boldsymbol{\sigma}_{\zeta},\boldsymbol{\Re}_{c},\Delta\boldsymbol{\varepsilon}_{\Re f}\right)\\ &\quad+\zeta\left(\left.\frac{\partial\sigma_{ij}^{\zeta}}{\partial\Re_{kl}^{\zeta}}\right|_{\boldsymbol{\Re}_c}O(\zeta)+\left.\frac{\partial\sigma_{ij}^{\zeta}}{\partial\Delta\varepsilon_{kl}^{\Re\zeta}}\right|_{\Delta\boldsymbol{\varepsilon}_{\Re c}}\Delta\varepsilon_{kl}^{\Re(1)}\right)\\ &= \sigma_{ij}^{(0)}\left({}_n\boldsymbol{\sigma}_{\zeta},\boldsymbol{\Re}_{c},\Delta\boldsymbol{\varepsilon}_{\Re f}\right)+\zeta\sigma_{ij}^{(1)}+O(\zeta^2)\end{aligned} \tag{16}$$

Further expanding Eq.(16) in Taylor's series around the unit cell centroid in the current configuration yields

$$\begin{aligned}\sigma_{ij}^{\zeta}(\boldsymbol{x},\boldsymbol{y},t) &= \sigma_{ij}^{(0)}(\hat{\boldsymbol{x}},\boldsymbol{y},t)+\left.\frac{\partial\sigma_{ij}^{(0)}}{\partial x_k}\right|_{\hat{\boldsymbol{x}}}(x_k-\hat{x}_k)+\zeta\sigma_{ij}^{(1)}(\hat{\boldsymbol{x}},\boldsymbol{y},t)+\zeta\left.\frac{\partial\sigma_{ij}^{(1)}}{\partial x_k}\right|_{\hat{\boldsymbol{x}}}(x_k-\hat{x}_k)\cdots\\ &= \underbrace{\sigma_{ij}^{(0)}(\hat{\boldsymbol{x}},\boldsymbol{y},t)}_{\sigma_{ij}^{f}(\hat{\boldsymbol{x}},\boldsymbol{y},t)}+\zeta\left(\left.\frac{\partial\sigma_{ij}^{(0)}}{\partial x_k}\right|_{\hat{\boldsymbol{x}}}y_k+\sigma_{ij}^{(1)}(\hat{\boldsymbol{x}},\boldsymbol{y},t)\right)+O(\zeta^2)\end{aligned} \tag{17}$$

Substituting Eq.(17) into equilibrium equation (1)a yields the two-scale equilibrium equations

$$\begin{aligned}&O\left(\zeta^{-1}\right):\ \sigma_{ij,y_j}^{f}(\hat{\boldsymbol{x}},\boldsymbol{y},t)=0\\ &O(1):\ \left.\frac{\partial\sigma_{ij}^{f}}{\partial x_j}\right|_{\hat{\boldsymbol{x}}}+\sigma_{ij,y_j}^{(1)}(\hat{\boldsymbol{x}},\boldsymbol{y},t)+b_i^{\zeta}(\hat{\boldsymbol{x}},t)=0\end{aligned} \tag{18}$$

Averaging Eq.(18)b over the deformed unit cell domain Θ_y gives the coarse-scale equilibrium equation

$$\begin{aligned}&\left.\frac{\partial\sigma_{ij}^{c}}{\partial x_j}\right|_{\hat{\boldsymbol{x}}}+b_i^{c}(\hat{\boldsymbol{x}},t)=0\\ &\sigma_{ij}^{c}(\hat{\boldsymbol{x}},t)=\frac{1}{|\Theta_y|}\int_{\Theta_y}\sigma_{ij}^{f}(\hat{\boldsymbol{x}},\boldsymbol{y},t)\,d\Theta_y\\ &b_i^{c}(\hat{\boldsymbol{x}},t)=\frac{1}{|\Theta_y|}\int_{\Theta_y}b_i(\hat{\boldsymbol{x}},\boldsymbol{y},t)\,d\Theta_y\end{aligned} \tag{19}$$

It is convenient to express the unit cell equilibrium equation (18)a in the corotational frame. Rewriting Eq.(18)a gives

$$\frac{\partial\sigma_{ij}^{f}}{\partial y_k^{\Re}}\frac{\partial y_k^{\Re}}{\partial y_j}=\frac{\partial\sigma_{ij}^{f}}{\partial y_k^{\Re}}\Re_{jk}^{c}(\hat{\boldsymbol{x}},t)=0$$

Multiplying above by $\Re^c_{il}(\hat{\boldsymbol{x}},t)$ yields

$$\left(\Re^c_{il}(\hat{\boldsymbol{x}},t)\Re^c_{jk}(\hat{\boldsymbol{x}},t)\sigma^f_{ij}\right)_{,y^{\Re}_k} \equiv \sigma^{\Re f}_{lk,y^{\Re}_k} = 0 \tag{20}$$

The Cauchy stress in the corotational frame $\sigma^{\Re f}_{ij}$ can be expressed in terms of converged value ${}_n\sigma^{\Re f}_{ij}$ and the new increment $\Delta\sigma^{\Re f}_{ij}$, which yields the following unit cell governing equations

$$\begin{aligned}
&\Delta\sigma^{\Re f}_{ij,y^{\Re}_j} = 0\\
&\Delta\sigma^{\Re f}_{ij} = L^{\Re}_{ijkl}\left(\Delta\varepsilon^{\Re f}_{kl} - \Delta\mu^{\Re f}_{kl}\right)\\
&\Delta\varepsilon^{\Re f}_{ij} = \Delta u^{\Re(1)}_{\left(i,y^{\Re}_j\right)} + \Delta\varepsilon^{\Re c}_{ij}\\
&\left[\!\left[\Delta\sigma^{\Re f}_{ij} n^{\Re}\right]\!\right]_{S^{\Re}} = 0\\
&\Delta u^{\Re(1)} - periodic
\end{aligned} \tag{21}$$

where $S^{\Re}$ denotes the interface between microconstituents; $[\![\cdot]\!]$ is a jump operator.

The incremental unit cell problem in the corotational frame Eq.(21) is solved by constructing the residual-free field similarly to [Oskay and Fish (2007); Oskay and Fish (2008); Yuan and Fish (2009)a,b; Fish and Yuan (2009), Fish, Filonova and Yuan (2013)] for small deformation problems

$$\begin{aligned}
\Delta u^{\Re(1)}_i(\hat{\boldsymbol{x}},\boldsymbol{y}) = \;& H^{kl}_i(\boldsymbol{y})\Delta\varepsilon^{\Re c}_{ij}(\hat{\boldsymbol{x}})\\
&+ \textstyle\int_{\Theta} \tilde{h}^{kl}_i(\boldsymbol{y},\tilde{\boldsymbol{y}})\,\Delta\mu^{\Re f}_{kl}(\hat{\boldsymbol{x}},\tilde{\boldsymbol{y}})d\tilde{\Theta}\\
&+ \textstyle\int_S \breve{h}^{\breve{n}}_i(\boldsymbol{y},\breve{\boldsymbol{y}})\,\Delta\breve{\delta}^{\Re f}_{\breve{n}}(\hat{\boldsymbol{x}},\breve{\boldsymbol{y}})d\breve{S}
\end{aligned} \tag{22}$$

with only exception that all the fields are expressed in the corotational frame. $\mu^{\Re f}_{kl}$ and $\breve{\delta}^{\Re f}_{\breve{n}}$ denote the leading order (fine-scale) eigenstrain and eigenseparation, respectively, in the corotational frame. The eigenstrain $\mu^{\Re f}_{kl}$ represents inelastic strain, thermal strain, moisture-induced strain, phase transformation, etc., when and if such material behaviour is present. The eigenseparation describes separation of material phases if this is present.

Model reduction is obtained by discretizing eigenstrains $\Delta\mu^{\Re f}_{kl}$ and eigenseparations $\Delta\breve{\delta}^{\Re f}_{\breve{n}}$ as in, for example, [Oskay and Fish (2007); Yuan and Fish (2009)a,b]

$$\begin{aligned}
\Delta\mu^{\Re f}_{kl}(\hat{\boldsymbol{x}},\boldsymbol{y}) &= \sum_{\alpha=1}^{\tilde{M}} \tilde{N}^{(\alpha)}(\boldsymbol{y})\mu^{(\alpha)}_{ij}(\hat{\boldsymbol{x}})\\
\Delta\breve{\delta}^{\Re f}_{\breve{n}}(\hat{\boldsymbol{x}},\boldsymbol{y}) &= \sum_{\xi=1}^{\breve{M}} \breve{N}^{(\xi)}(\boldsymbol{y})\breve{\delta}^{(\xi)}_{\breve{n}}(\hat{\boldsymbol{x}})
\end{aligned} \tag{23}$$

Subsequently the influence function H_i^{kl}, $\tilde{h}_i^{kl}$, $\breve{h}_i^{\breve{n}}$ are computed by substituting discretization into the equilibrium equation (21) a and requiring arbitrariness $\mu_{ij}^{(\alpha)}(\hat{\boldsymbol{x}})$ and $\delta_{\breve{n}}^{(\xi)}(\hat{\boldsymbol{x}})$.The three influence function problems solved priori to macroscopic analysis [see Oskay and Fish (2007); Yuan and Fish (2009)a,b].

Finally, the reduced order equations for eigenfields, $\mu_{ij}^{(\alpha)}(\hat{\boldsymbol{x}})$ and $\delta_{\breve{n}}^{(\xi)}(\hat{\boldsymbol{x}})$, is obtained by satisfying phase constitutive equations and traction continuity (for details see [Oskay and Fish (2007); Oskay and Fish (2008); Yuan and Fish (2009)a,b; Fish and Yuan (2009)].

Remark 1: In the case of large unit cell distortion the influence functions H_i^{kl}, $\tilde{h}_i^{kl}$, $\breve{h}_i^{\breve{n}}$ have to be recomputed from time to time. One possible measure of tracking unit cell deformation is to track its dilatational (volume change) or distortional (shape change) measures. The magnitude of the dilatational deformation can be measured by the third invariant of the coarse-scale deformation gradient (or coarse-scale Jacobian). The magnitude of the distortional deformation can be tracked by von Mises coarse-scale Green-Lagrange strain.

It is, however, instructive to point out that if the unit cell geometry is changing considerably from one load increment to another, the reduced order homogenization outlined here would offer little advantage over nonlinear direct homogenization approach. Moreover, an approximation in Eq.(7) may no longer be accurate. Instead, a phase rotation, $\Re_{ki}^{(\alpha)}(\hat{\boldsymbol{x}},t)$, that tracks an average rotation of each phase has to be defined.

Given equations (21) and (22) the process of constructing and solving the residual-free equations in the corotational frame is identical to that considered for small deformation problems [Oskay and Fish (2007); Oskay and Fish (2008); Yuan and Fish (2009)a,b; Fish and Yuan (2009); Fish, Filonova and Yuan (2013)]. Once the fine-scale stress in the corotational frame $\sigma_{ij}^{\Re f}$ has been computed, the coarse-scale stress $\sigma_{ij}^{\Re c}$ in the corotational frame is computed by averaging $\sigma_{ij}^{\Re f}$. The resulting coarse-scale stress in the global Cartesian coordinate is computed by rotating the coarse-scale stress from the corotational frame

$$\sigma_{ij}^{c}({}^{i+1}_{n+1}\hat{\boldsymbol{x}}) = \Re_{il}^{c}({}^{i+1}_{n+1}\hat{\boldsymbol{x}})\,\Re_{jk}^{c}({}^{i+1}_{n+1}\hat{x})\,\sigma_{lk}^{\Re c}({}^{i+1}_{n+1}\hat{\boldsymbol{x}}) \tag{24}$$

Remark 2: Construction of the tangent stiffness matrix requires linearization of the rotational matrix $\Re_{jk}^{c}$ computed at the mid-step and at the end of the increment at each Newton iteration. Since $\Re_{jk}^{c}$ is assumed not to depend on the fine-scale problem its construction and linearization are governed by the deformation of the coarse-scale problem only. The interested reader is referred to Rankin (1988) for more details.

Remark 3: For composite plate or shells elements, it is necessary to enforce plane stress condition on the unit cell. This can be accomplished in one of the three ways. One possibility is to conduct a three-scale asymptotic homogenization approach along the lines proposed by Caillerie (1984) and Kohn and Vogelius (1984). The three-scale asymptotic homogenization method has been recently applied by Oskay and Pal (2010) to reduced order homogenization. By this approach, the microstructure is assumed to be periodic in the plane of the plate or shell, whose thickness is assumed to be infinitesimally small, i.e., of the same order of magnitude to the unit cell in-plane dimensions. The second possibility is to assume that the unit coarse-scale strain component ε^c_{33} is unknown and to impose the overall coarse-scale stress component σ^c_{33} to vanish (subscript 3 denotes the direction normal to the plate or shell surface). Furthermore, elastic properties and influence functions have to be modified to enforce vanishing normal stress component. Finally, the third and the simplest variant entails letting the nodes on the unit cell boundary normal to the surface of the plate to be free except for constraining the rigid body motion of the unit cell. In this latter scenario, the unit cell is subjected five overall deformation modes excluding ε^c_{33}.

3 Model validation

The reduced order homogenization method, where the coarse-scale fields are driven by damage accumulation in the microstructure, is employed for spatial upscaling and model reduction. Three different random inclusion microstructures are considered. The implementation involves microscale analysis wherein the unit cell problem with periodic boundary conditions is solved and a macroscale analysis wherein the macroscale quantities of interest, such as stresses, are computed from the fine-scale.

The microscale analysis consists of four steps as enumerated below:

1. Unit cell definition: This step consists of generating unit cell geometry, finite element mesh, assigning local material coordinate system and defining periodic boundary conditions;

2. Characterization of linear material properties: In this step, linear properties of micro phases are characterized (identified) by solving a nonlinear least squares problem which minimizes the error between the computed and experimental elastic properties of micro-phases. Note that in situ properties of phase materials in the composite can be vastly different from those obtained in the experiments of individual micro phase materials. This is due to defects developed during manufacturing process, shape changes and so on;

3. Computation of the reduced order model influence functions: This step involves solving the eigenstrain and eigenseparation influence functions and computing coefficient tensors that are stored in a material database required to solving the nonlinear unit cell problem in Step 4;

4. Characterization of nonlinear material properties: This step involves characterization of nonlinear phase properties by solving a least square problem.

3.1 Randomly distributed chopped fiber composite in two-dimensional plane

We consider statistically representative chopped fiber composite unit cell depicted in Figure 3a. Procedures of automated construction of the unit cell model are described in [Bailakanavar, Liu, Fish, and Yuan (2012)]. Material properties (Young's modulus, Poisson ratio and strength) of the micro constituents are depicted in Tab. 1.

Table 1: Properties of the phases comprising the chopped fiber composite unit cell [Bailakanavar, Liu, Fish, and Yuan (2012)]

Phase	E(GPa)	ν	S (MPa)
resin	3.5	0.3	95
carbon fiber	230	0.25	4200

For model validation, we consider a three-point bending experiment conducted at General Motors. Multiscale analysis is conducted with MDS [Multiscale Design Systems] linked with LsDyna UMAT50 [LS-DYNA] as a macro-solver. The beam has a hat section and is supported by two fixed rollers at either end and a moving roller in the middle as show in Figure 3b,c. The beam is discretized with quadrilateral shell elements with single in-plane point integration and seven through-the-thickness integration points. Crack initiation and propagation is implemented by invoking the element deletion criterion in LsDyna. The criterion for element deletion is based on the damage in the resin phase.

The force-displacement curve as obtained using multiscale simulation is compared to the experimental data in Fig.4. It can be seen that the numerical simulation is in good agreement with the experimental data.

3.2 Randomly distributed 'soft' and 'hard' domains in a high-density polyethylene

Here we consider an impact of a projectile on a steel plate coated by a high-density polyethylene (HDPE). The microstructure of the polymer comprises of randomly

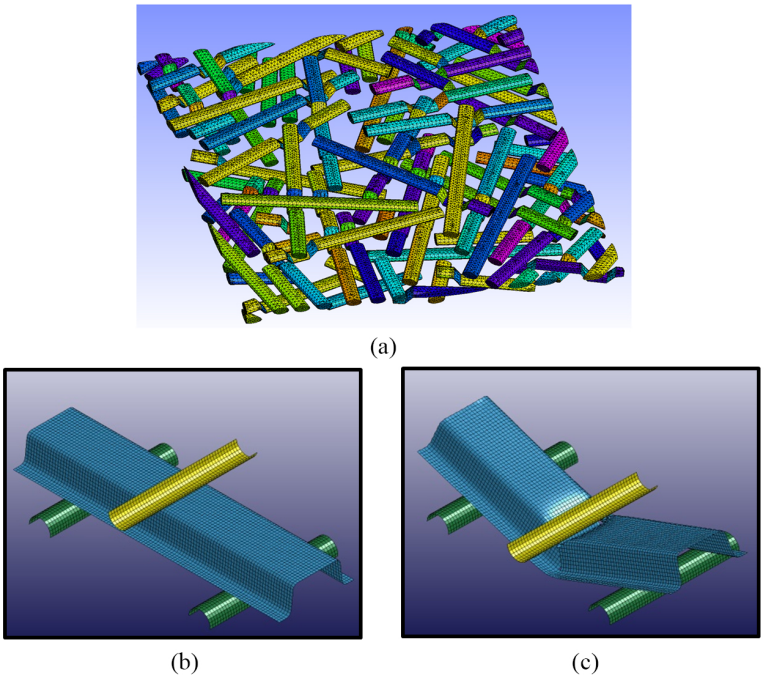

Figure 3: (a) Statistically representative chopped fiber composite microstructure with only tows shown (35% tow volume fraction) (b) three-point bending test set up (c) completely damaged hat section beam

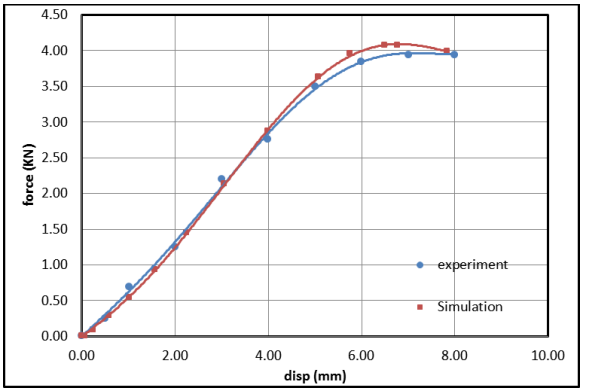

Figure 4: Force-displacement curve. Comparison of simulation and experimental results for three-point bending test.

segmented copolymers composed of 'hard' domains and 'soft' domains forming a two-phase microstructure as shown in Table 1. The micro phase separation of 'hard' and 'soft' domains is responsible for the versatile properties of the broad class of polymers, but also raises the computational challenges in studying the properties of these material [Petrovic and Ferguson (1991)].

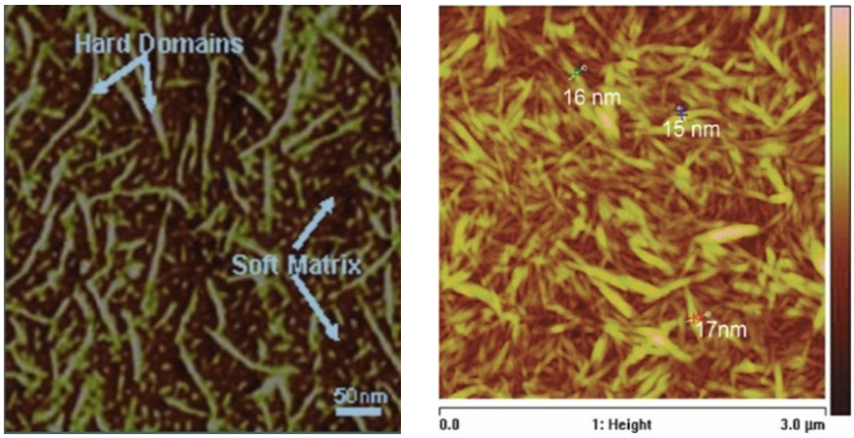

(a) (b)

Figure 5: (a) Osmium tetroxide tainted thermoplastic polyurethanes (57% of 'soft' segments and 43% of 'hard' segments) [Grujicic, He, Pandurangan, Svingala, Settles, and Hargather (2012)]; (b) height image of the nanowhiskers showing the diameter measurements of the cellulose nanowhiskers [Goetz, Foston, Mathew, Oksman, and Ragauskas (2010)]

A combination of displacement controlled quasi-static simulations is conducted to calibrate the material properties of the phases comprising the HDPE microstructure. Multiscale simulations are based on reduced order homogenization method [Multiscale Design Systems]. Both phases are described by a viscoplasticity model based on overstress (VBO) [Cernocky and Krempl (1979); Yuan, Ruggles-Wrenn, and Fish (2013)]. The nonlinear phase properties are identified with respect to experimental data available in [Zhang and Moore (1997)a; Zhang and Moore (1997)b]. Figure 3 shows the stress-strain results for the isotropic configuration of the unit cell.

Multiscale simulations of the response of a circular sandwich plate subjected to a dynamic impact loading by a half an inch fragment simulating projectile (FSP) are summarized below. The sandwich structure comprises of a DH-36 steel target plate

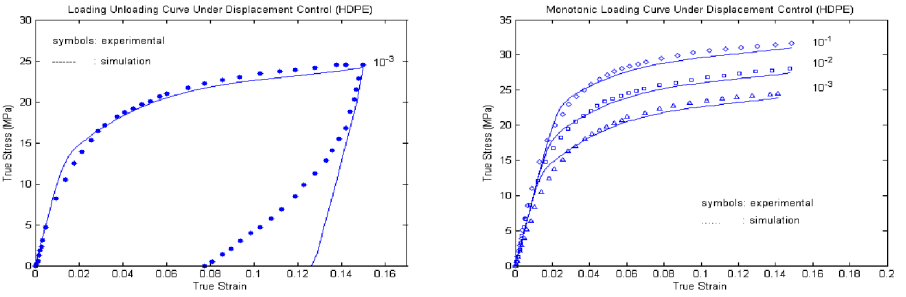

Figure 6: Quasi-static stress-strain curves. Simulation results are calibrated for isotropic HDPE material with'hard' and 'soft' domains described by VBO model.

placed at the outer front layer with a backside polymer layer (HDPE) glued to the steel by epoxy. DH-36 steel is modeled using Johnson-Cook constitutive model along with Johnson-Cook failure criteria. The backside coating polymer material is modeled as a two-phase composite with 'hard' inclusions and 'soft' matrix. Both phases are described by VBO model as discussed above. The geometric configuration of the sandwich plate is illustrated in Figure 7. Due to symmetry, only a quarter of the plate is modeled. The FSP is modeled as a discrete rigid body with an initial velocity of 407m/s.

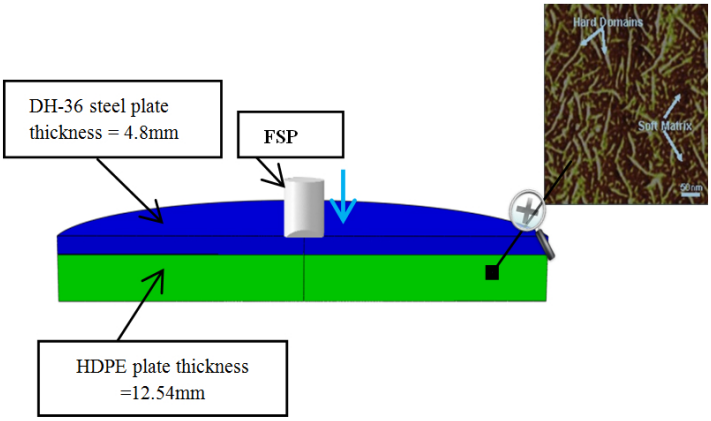

Figure 7: DH-36 steel and HDPE sandwich structure simulation setup.

To study the role of heterogeneity and anisotropy on energy absorption in steel/HDPE plates, two types of random ellipsoidal inclusion unit cells with 20% volume frac-

tion of 'hard' domains are considered. The first microstructure of the HDPE unit cell consists of 'hard' domains (approximated by ellipsoidal inclusions) randomly distributed in a 'soft' domain resulting in macroscopically isotropic behavior. The second microstructure has ellipsoidal inclusions preferentially oriented at a 45-degree angle with respect to the loading direction in attempt to dissipate the energy via shear wave. The architecture of the two composite microstructures is shown in Figure 8.

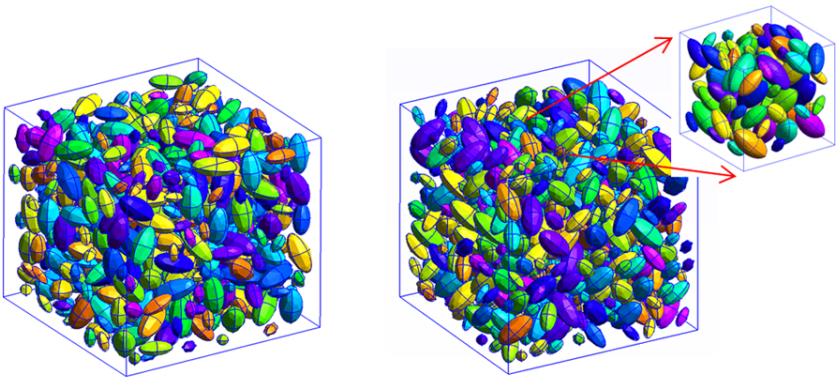

(a) isotropic case (b) anisotropic case

Figure 8: (a) Random and (b) preferentially packed 'hard' domains in the HDPE microstructure. Volume fraction of 'hard' domains is 20%.

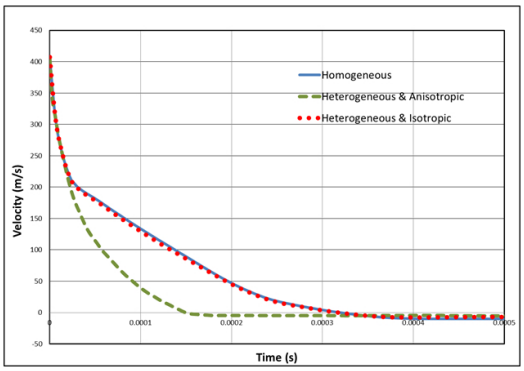

Figure 9: Velocity decay curve of the projectile impacted to the steel/polymer plate. Comparison of simulation results for isotropic, anisotropic and homogeneous polymer microstructures.

The FSP velocity decay curves for the two microstructures are shown in Figure 9. It is evident that preferential orientation of the ellipsoidal inclusions enhances the energy absorption of the composite plate. It is also evident that it is possible to identify single-scale phenomenological material properties of HDPE that would result in a similar behavior obtained from the two-scale model.

3.3 Randomly distributed fibers in Phenolic Resin

Phenolic Impregnated Carbon Ablators (PICA) finds its application in the aerospace industry. It is used as a heat shield on spacecrafts to prevent structural damage during reentry in to the atmosphere. The microstructure of fiber framework called *fiberform* with a high thermal conductivity is embedded in an amorphous matrix with low thermal conductivity [Agrawal and Chavez-Garcia (2011)], Fig. 10. The carbon fibers are oriented preferentially in one plane, making it a transverse isotropic material with different material properties in through-the-thickness and in-plane directions. In this study, we model the microstructure of PICA with randomly distributed fibers in 3D space bounded by the amorphous resin material. The fibers are preferentially oriented at a 90-degree angle with respect to the out-of-plane direction as is shown in Figure 11.

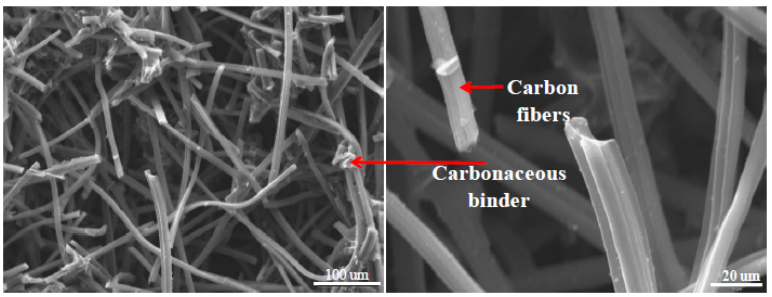

Figure 10: Microstructure of PICA [Agrawal and Chavez-Garcia (2011)].

The multiscale simulations using reduced order homogenization of uniaxial tension tests are conducted for un-notched and notched specimens [Agrawal and Chavez-Garcia (2011)]. Fibers are modeled as linear elastic, and the amorphous resin is described using a piecewise linear continuum damage mechanics model as shown in Figure 12. The uniaxial tensile test involving an un-notched specimen is conducted to identify the properties of the fiber phenolic resin by solving a nonlinear inverse problem. The identified phase properties for fiber and matrix are listed in Tab. 2 and Tab. 3, respectively, the comparison with the experiment is given in Fig. 14.

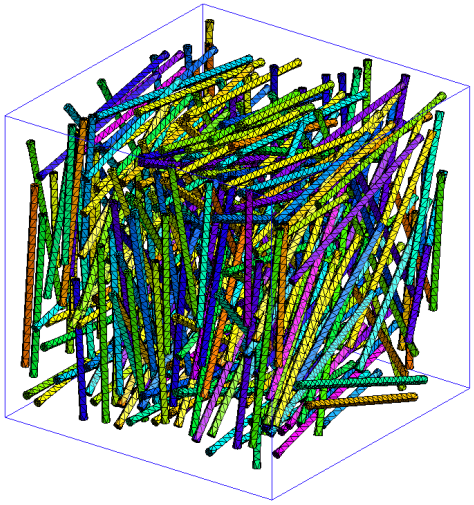

Figure 11: PICA unit cell geometry

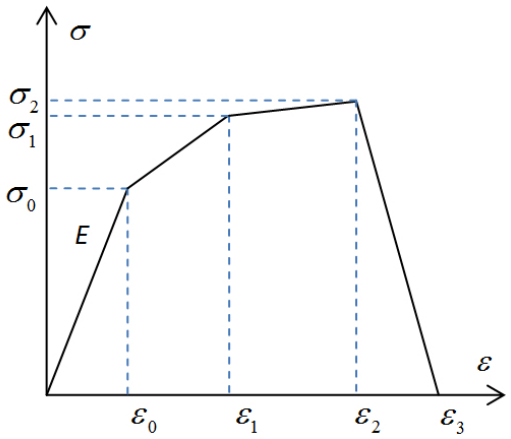

Figure 12: Piecewise linear damage model for resin

Table 2: Characterized properties of fiber

E (GPa)	ν
23	0.25

Table 3: Characterized properties of resin

E(GPa)	ν	σ_0(MPa)	σ_1 (MPa)	ε_1	σ_2 (MPa)	ε_2	ε_3
0.267	0.3	0.089	0.410	0.0107	0.485	0.0145	0.015

The identified elastic properties of carbon fibers and the tensile strength of the resin are about 10 times smaller than those reported in the literature.

Remark 4: In a composite material the reduced fiber stiffness in comparison to elastic straight fibers is due to either fiber curvature (see [Farsadi et al (2012), Gonsales, llorca (2005)] or due to manufacturing defects. This reduction in fiber stiffness is taken into account by identifying (calibrating) fiber properties to yield experimental results of the composite in uniform field tests. A similar approach has been employed in [Farsadi et al (2012)] where the waviness of nanotubes embedded in a polymer caused a decrease in the longitudinal and transverse Young's modulus of composites compared to the straight nanotube reinforcement, and in [Gonsales, llorca (2005)] where the modulus of the polyethylene felts has been reduced by two orders of magnitude due to fiber folding in comparison to straight fibers.

The decrease of pure resin properties can be explained by existence of porosity in the real composite.

The finite element model of the notched specimen and the value of damage parameter in the resin phase are shown in Figure 13. It can be seen that the crack propagates along a straight-line through the thickness of the specimen. The resulting stress-strain curves for the notched specimen are compared with the experimental results in Figure 15. The simulation results are found to be in good agreement with the experimental results.

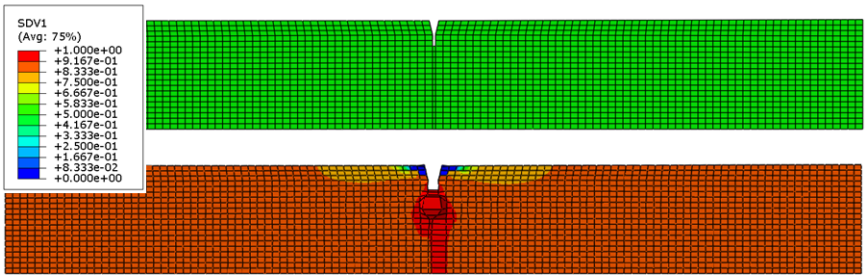

Figure 13: Uniaxial tensile test setup for notched specimen

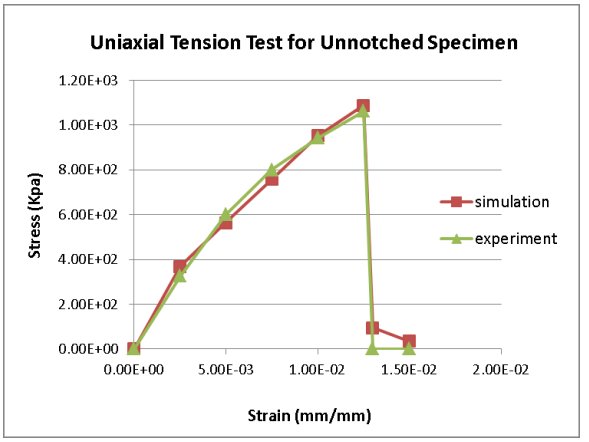

Figure 14: Model identification - stress-strain results for PICA in un-notched specimen.

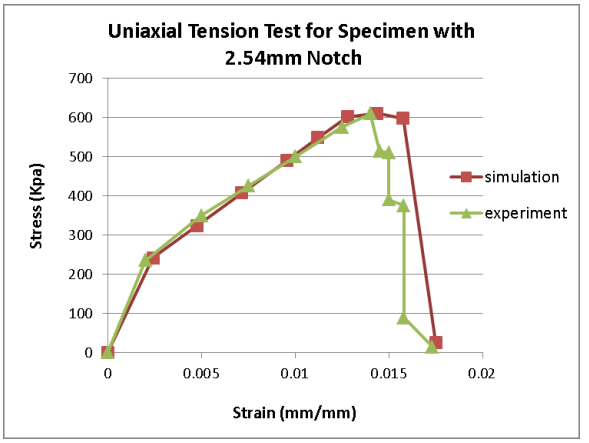

Figure 15: Model validation - stress-strain curve for PICA in specimen with 2.54mm notch.

3.4 Fiberform

Fiberform is a very porous low-density carbon fiber insulation material designed for high temperatures applications. It consists of a group of carbon fibers bonded to each other (Fig. 16) by means of an organic binder that is carbonized at very high temperature. The fiberform unit cell is generated based on the algorithm developed in [Bailakanavar, Liu, Fish, and Yuan (2012)]. The fibers are modeled as linear elastic and their properties are given in Table 2. The binders are described using

the piecewise damage model depicted in Fig. 12. The identified binder model parameters based on un-notched specimens [Agrawal and Chavez-Garcia (2011)] are given in Table 4 and the comparison with the experiment is given in Fig. 17.

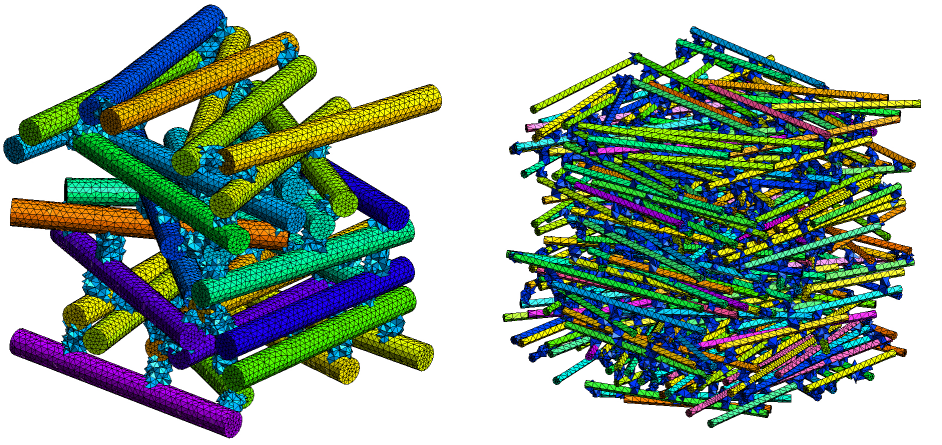

(a) (b)

Figure 16: Fiberform unit cell with: (a) fiber volume fraction 5% and an aspect ratio (between fiber length and cross-section diameter) 35:4.8; (b) fiber volume fraction 10% and an aspect ratio 10:1.2. The latter is used in simulations.

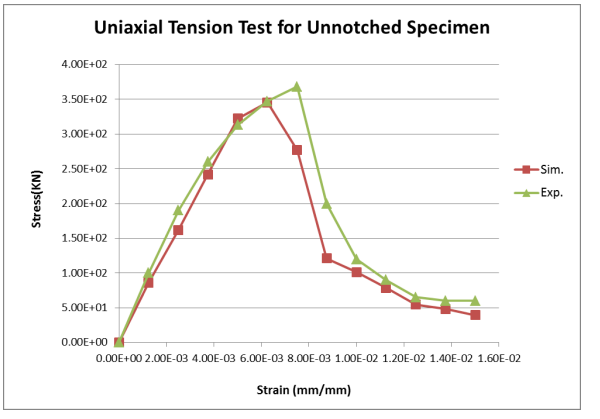

Figure 17: Model identification - stress-strain results for fiberform in un-notched specimen

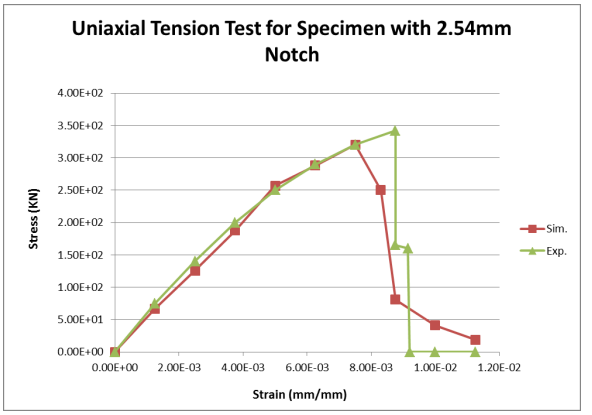

Figure 18: Model validation - stress-strain curve for fiberform in specimen with 2.54mm notch.

Table 4: Elastic and damage material properties for binders

E(GPa)	ν	σ_0(MPa)	σ_1 (MPa)	ε_1	σ_2 (MPa)	ε_2	ε_3
23	0.25	1	0.66	0.001	0.036	0.02	0.05

The simulation results of uniaxial tension for the notched specimens are compared with the experiments [Agrawal and Chavez-Garcia (2011)] as shown in Fig. 18. An appropriate agreement has been observed between the numerical simulation results and the experimental data. The discrepancies in the peak response can be a result of errors in the mathematical model, discretization and material defects. From the practical point of view, the numerical results are considered to be sufficiently accurate.

4 Conclusion

In this manuscript, we develop a corotational form of the reduced order homogenization approach. The corotational framework allows accounting for large deformations, associated with large rotations and moderate unit cell strains. The computational efficiency of the reduced order homogenization (with appropriate loss of accuracy) in comparison with the direct homogenization method is obtained by precomputing linear homogenized material properties and eigenstrain influence functions at a fine scale prior to conducting nonlinear coarse-scale analysis. The proposed corotational form of the reduced order homogenization is validated on four numerical examples, which show good agreement with experimental data.

References

Agrawal, P.; Chavez-Garcia, J.F. (2011): Fracture in phenolic impregnated carbon ablator. *In 42nd AIAA Thermophysics Conference. Honolulu, Hawaii*.

Argyris, J. H. (1982): An excursion into large rotations. *Comp. Meths. Appl. Mech. Engrg*., vol. 32, pp. 85–155.

Bailakanavar, M.; Liu, Y.; Fish J.; Yuan Z. (2012): Automated modeling of random inclusion composites. *Engineering with Computers*. DOI 10.1007/s00366-012-0310-x.

Belytschko,T.; Hsieh, B. J. (1973): Nonlinear transient finite element analysis with convected coordinates. *Int. J.Numer. Meth. Engrg*., vol. 7, pp. 255-271.

Bergan, P. G.; Horrigmoe, G. (1976): Incremental variational principles and finite element models for nonlinear problems. *Comp. Meths. Appl. Mech. Engrg*., vol. 7, pp. 201–217.

Caillerie, D. (1984): Thin Elastic and Periodic Plates. *Math. Meth. Appl. Sci.*, vol. 6, no. 3, pp. 159–191.

Farsadi, M.; Ochsner, A.; Rahmandoust, M. (2012): Numerical investigation of composite materials reinforce with waved carbon. *J. Compos. Mater.*, DOI: 10.1177/0021998312448495.

Fish, J.; Yuan, Z. (2008): *Bridging the Scales in Science and Engineering*; in J. Fish (ed). Oxford University Press.

Fish, J. ; Filonova ,V.; Yuan, Z. (2013): Hybrid impotent-incompatible eigenstrain based homogenization. *Int. J. Numer. Meth. Engng*., vol. 95, no.1, pp. 1-32.

Fish, J. ; Shek, K. L. (2000): Finite Deformation Plasticity Based on the Additive Split of the Rate of Deformation and Hyperelasticity. *Comp. Meth. Appl. Mech. Engng.,* vol. 190, pp. 75-93.

Goetz, L.; Foston, M.; Mathew, A.P.; Oksman, K.; Ragauskas, A.J. (2010): Poly(methyl vinyl ether-co-maleic acid)-polyethylene glycol nanocomposites cross-linked in situ with cellulose nanowhiskers. *Biomacromolecules*, vol. 11, no.10, pp. 2660-2666.

Gonzalez, C.; LLorca, J. (2005): Stiffness of a curved beam subjected to axial load and large displacements. *Int. J. Solids Struct.*, vol. 42, pp. 1537-1545.

Grujicic, M.; He, T.; Pandurangan, B.; Svingala, F.R.; Settles, G.S.; Hargather, M.J. (2012): Experimental characterization and material-model development for microphase-segregated polyurea. *J Mat Engg & Perf*, vol.21, no. 1, pp. 2-16.

Kohn, R.V.; Vogelius, M. (1984): A New Model for Thin Plates with Rapidly

Varying Thickness. *Int. J. Solids Struct.*, vol. 20, no. 4., pp. 333–350.

LS-DYNA. http://www.lstc.com/products/ls-dyna

Multiscale Design Systems, www.multiscale.biz

Oskay, C.; Fish, J. (2007): Eigendeformation-Based Reduced Order Homogenization. *Comp. Meth. Appl. Mech. Engng.*, vol. 196, pp. 1216-1243.

Oskay, C.; Fish, J. (2008): Fatigue Life Prediction using 2-Scale Temporal Asymptotic Homogenization. *Comput. Mech.*, vol. 42, no. 2, pp. 181-195.

Oskay, C.; Pal, G. (2010): A Multiscale Failure Model for Analysis of Thin Heterogeneous Plates. *Int. J. Dam. Mech.*, vol. 19, pp.575-610.

Petrovic, Z.N.; Ferguson, J. (1991): Polyurethane elastomers. *Programmable Polymer Science*, vol. 16, pp. 695-836.

Rankin, C. C. (1988): Consistent linearization of the element-independent corotational formulation for the structuralanalysis of general shells. *NASA Contractor Report 278428, Lockheed Palo Alto Research Laboratory, Palo Alto, CA*

Yuan, Z.; Fish, J. (2009)a: Multiple Scale Eigendeformation-Based Reduced Order Homogenization. *Comp. Meth. Appl. Mech. Engng.*, vol. 198, no.21-26, pp. 2016-2038.

Yuan, Z.; Fish, J. (2009)b: Hierarchical Model Reduction at Multiple Scales. *Int. J. Numer. Meth. Engng*, vol. 79, pp. 314-339.

Yuan , Z.; Ruggles-Wrenn , M.; Fish , J. (2013): Computational viscoplasticity based on overstress (CVBO) model. To appear in *Int. J. Comp. Engg. Sci*.

Zhang, C.T.; Moore, I.D. (1997)a: Nonlinear mechanical response of high density polyethylene Part 1. Experimental investigation and model evaluation. *Polymer Eng. Sci.*, vol. 37, no. 2, pp. 404-413.

Zhang, C.T.; Moore, I.D. (1997)b: Nonlinear mechanical response of high density polyethylene Part 2. Uniaxial constitutive modeling. *Polymer Eng. Sci.*, vol. 37, no. 2, pp. 414-420.